

From fish to fiber: 3D-nanoprinted optical neuromast for multi-integrated underwater detection

Received: 9 September 2024

Accepted: 22 July 2025

Published online: 11 August 2025



Liangye Li^{1,4}, Xuhao Fan^{2,4}, Geng Chen¹, Yueqi Liu¹, Fujun Zhang¹, Zhuolin Chen¹, Zhi Zhang¹, Wangyang Xu¹, Shixiong Zhang¹, Yuncheng Liu², Zongjing Li², Hui Gao^{2,3}, Zhijun Yan¹, Wei Xiong^{2,3}✉ & Qizhen Sun¹✉

Fish possess high sensitivity to acoustic, vibrational, and hydrodynamic stimuli through unique sensing cells, providing unparalleled paradigms for developing underwater detection methods. However, artificial perception devices face challenges in replicating comparable sensitivity and multi-dimensional integration of fish in function and scale. Here, we propose a biomimetic optical fiber neuromast (BOFN) by leveraging synergistic optical-mechanical interactions for multifunctional underwater detection and communication. A heterogeneous integration technology for BOFN is developed based on sequential femtosecond laser direct writing with deposition, resulting in both compact size and reliable stability. Benefiting from its biomimetic design, BOFN demonstrates performance benchmarks in acoustic sensitivity of 172.24 V/kPa and marine turbulence sensitivity of 8560.72 nm/(m/s). A prototype system integrated into a motorized fish shows versatile acoustic sensing, target imaging, and underwater communication capabilities. Our work opens avenues for deploying all-optical bionic sensing cells in underwater environments, with promising applications in marine resource exploration and ecosystem protection.

Underwater acoustic, vibrational, and water flow signals hold a wealth of information essential to exploring the vast and largely uncharted ocean. These signals provide critical data for underwater early warning^{1,2}, sonar detection^{3,4}, uncharted navigation^{5,6}, and encrypted communications^{7,8}, making versatile underwater sensing crucial for marine resource exploration and ecological protection. In nature, fish has evolved a specialized sensory organ known as the lateral line, which enables them to detect water currents, sounds, and vibrations with remarkable sensitivity and multi-dimensional integration in function and scale^{9–11}. This high performance is attributed to the unique structure of the lateral line system. When water enters the lateral line tube through its pores, the neuromast, which is comparable

in size to a cell, captures external stimuli and transmits them to the nerve center via sensory nerve fibers. The integrated structure of pores, neuromasts, and nerves allows fish to perform real-time and versatile sensing in a highly sensitive and miniaturized way^{12,13}. Inspired by this biological model, efforts in underwater perception technology are increasingly focused on achieving functional integration and size reduction to replicate the effectiveness of the fish lateral line system.

Despite significant efforts in developing sensitive underwater perception systems, replicating the superior multi-dimensional integration of fish lateral lines in function and scale remains a formidable challenge. Recent advancements in hydroacoustic and water flow detection, including piezoelectric^{14,15}, piezoresistive^{16,17}, capacitive and

¹National Engineering Research Center for Next Generation Internet Access System (NGIA), School of Optical and Electronic Information, Huazhong University of Science and Technology, Wuhan, Hubei, China. ²Wuhan National Laboratory for Optoelectronics, Huazhong University of Science and Technology, Wuhan, Hubei, China. ³Optics Valley Laboratory, Wuhan, Hubei, China. ⁴These authors contributed equally: Liangye Li, Xuhao Fan. ✉e-mail: weixiong@hust.edu.cn; qzsun@mail.hust.edu.cn

resonator^{18,19}, optical fiber grating^{20–22}, and optical interferometer types^{23–26}, have shown promising performance. However, these systems are generally limited to performing a single function. Achieving multifunctionality often requires multiplexing of several sensing units, which significantly increases the size of the system and hinders its overall integration. To achieve scale integration for underwater sensing, various nano-fabrication techniques have been explored, such as micro-electromechanical systems (MEMS) processing technology and two-photon polymerization (TPP) techniques^{27–29}. Although device miniaturization has been studied, the current sensing structures remain vulnerable to water infiltration and other disturbances in the aquatic environment, resulting in low stability and short lifespans in conditions of electromagnetic interference, corrosive elements, and biological attachments. Therefore, a long-standing gap still exists for artificial devices and biological organisms in high-performance underwater sensing, demanding innovative solutions that simultaneously advance detection principles and manufacturing technologies.

Inspired by the structure and versatile sensing abilities of fish lateral lines, we propose a highly sensitive and multi-dimensional integrated biomimetic optical fiber neuromast (BOFN) capable of detecting ultrasonic signals, marine turbulence, and tiny vibrations. The biomimetic device consists of an optical fiber, an optical supporting cell, and an optical cilium. This design introduces a dual-sensitization mechanism by combining Fabry-Pérot (FP) interference with cantilever beam sensitization, which significantly enhances both detection sensitivity and accuracy. The optical supporting cell and optical cilium are 3D printed directly onto an optical fiber tip using a heterogeneous integration technique. Benefiting from the unique biomimetic sensing structure, optical fiber neuromast exhibits sensitive mechanical stimulus-response and broad-angle responsiveness, achieving an acoustic sensitivity of 172.24 V/kPa, marine turbulence velocity sensitivity of 8560.72 nm/(m/s), and a wide detection angle of 0–180°. The operational mechanism of the BOFN is based on synergistic optical-mechanical interactions within the biomimetic neuromast formed by the optical cilium and supporting cell. This design enables the BOFN to detect subtle changes in the underwater environment with high precision. Moreover, the BOFN can sensitively detect tiny vibrations and Morse code signals, enabling underwater communication. As a proof of concept, we construct an artificial fish lateral line system for a motorized fish, demonstrating simultaneous measurement of acoustic and water flow signals. This system also showcases the capability for underwater object imaging, which is significant in target recognition. The biomimetic design of this work enables sensitive and multi-integrated detection, highlighting its potential for underwater perception, marine security, and resource exploration.

Results

Biomimetic optical fiber neuromast (BOFN) inspired by the fish lateral line

The lateral line is a distributed array of biological sensors extending along the body of fish from head to tail^{30,31}. Water enters the lateral line tube through its pores, impacting the neuromast for real-time, highly sensitive sensing (Supplementary Fig. 1). The fish lateral line comprises a functional unit known as the canal neuromast³², which covers the head and body, positioned at or near the surface of the skin. The canal neuromast contains cilium, supporting cells, and nerve fibers (Fig. 1a). Cilium comprises kinocilium and stereocilia. The ciliary bundles of the hair cell are encased within a gelatinous structure known as the cupula. Water movement deflects the cupula, which in turn deflects the ciliary bundles, changing the membrane potential of the hair cells. Subsequently, nerve fibers transmit the potential change to the nerve center. Inspired by the fish lateral line, we designed the BOFN. Figure 1b shows the structure of the optical fiber neuromast. Similarly to the fish

neuromast, the fiber neuromast consists of the optical cilium, optical supporting cell, and optical fiber. The optical cilium and optical supporting cell function as the sensing unit, while the optical fiber is used for transmitting. Thus, the BOFN converts mechanical signals into optically detectable ones. The BOFN demonstrates high sensitivity in detecting acoustic signals, marine turbulence, and disturbance signals from uncrewed underwater vehicles (UUV) and organisms. It also creates an artificial fish lateral line, enabling a biomimetic robotic fish to perform underwater sensing tasks (Fig. 1b).

The operational mechanism is based on the synergistic optical-mechanical interactions within the biomimetic neuromast formed by the optical cilium and supporting cell. This introduces a dual-sensitization mechanism by combining FP interference with cantilever beam sensitization^{33,34}. Assuming the reflected intensities of the optical supporting cell surfaces are I_1 and I_2 , respectively, the interference signal I can be described as:

$$I = I_1 + I_2 + 2\sqrt{I_1 \cdot I_2} \cdot \cos\left(\frac{4\pi nL}{\lambda} + \varphi_0\right) \quad (1)$$

Here, n , λ , L , and φ_0 represent the refractive index of the supporting cell, the incident light wavelength, the cavity length, and the initial phase of the interference, respectively. Initially, the spectral interference produced by the optical supporting cell is determined by the geometry of the cavity. When mechanical stimuli are applied, the cilium deflects, which can be considered the deformation of a cantilever beam under a line load³⁵. The fluid-induced elastic deflection of the cilium and mechanical pressure acting directly on the diaphragm modify the length change of cavity ΔL . The total length change can be given by:

$$\Delta L = \Delta L_x + \Delta L_y \quad (2)$$

ΔL_x signifies the change in cavity length due to vertical mechanical pressure on the diaphragm of the supporting cell, while ΔL_y denotes the change in length in the supporting cell from the deflection of the cantilever beam. The relationship between ΔL_x and the pressure P_x is:

$$\Delta L_x = \frac{3(1 - \nu^2)D^4}{256Et^3} P_x \quad (3)$$

ν and E denote the Poisson ratio and the Young's modulus of the supporting cell, respectively. The variable P_x represents the exerted mechanical pressure acting in the vertical direction, while D and t correspond to the diameter and thickness of the supporting cell, respectively. ΔL_y satisfies the following equation:

$$\Delta L_y = H_1 - H_1 \sqrt{1 - \left(\frac{W}{H_1}\right)^2} \quad (4)$$

H_1 and H_2 are the lengths of the support cell and cilium, respectively. W is the deflection of the supporting cell, which nearly satisfies the deflection equation:

$$W = \frac{q_1 H_1^4}{8EI_s} + \frac{q_2 H_2 H_1^3}{3EI_s} + \frac{q_2 H_2^2 H_1^2}{4EI_s} \quad (5)$$

Here, q_1 and q_2 are the line loads on the supporting cell and optical cilium, I_s is the moment of inertia of the supporting cell. The length change ΔL of the supporting cell cavity results in a spectral shift $\Delta\lambda$ ³⁶. In the micro-optical supporting cell interferometer, the dip wavelength shift ($\Delta\lambda$) and the length change (ΔL) have the following relationship:

$$\frac{\Delta\lambda}{\lambda} = \frac{\Delta L}{L} \quad (6)$$

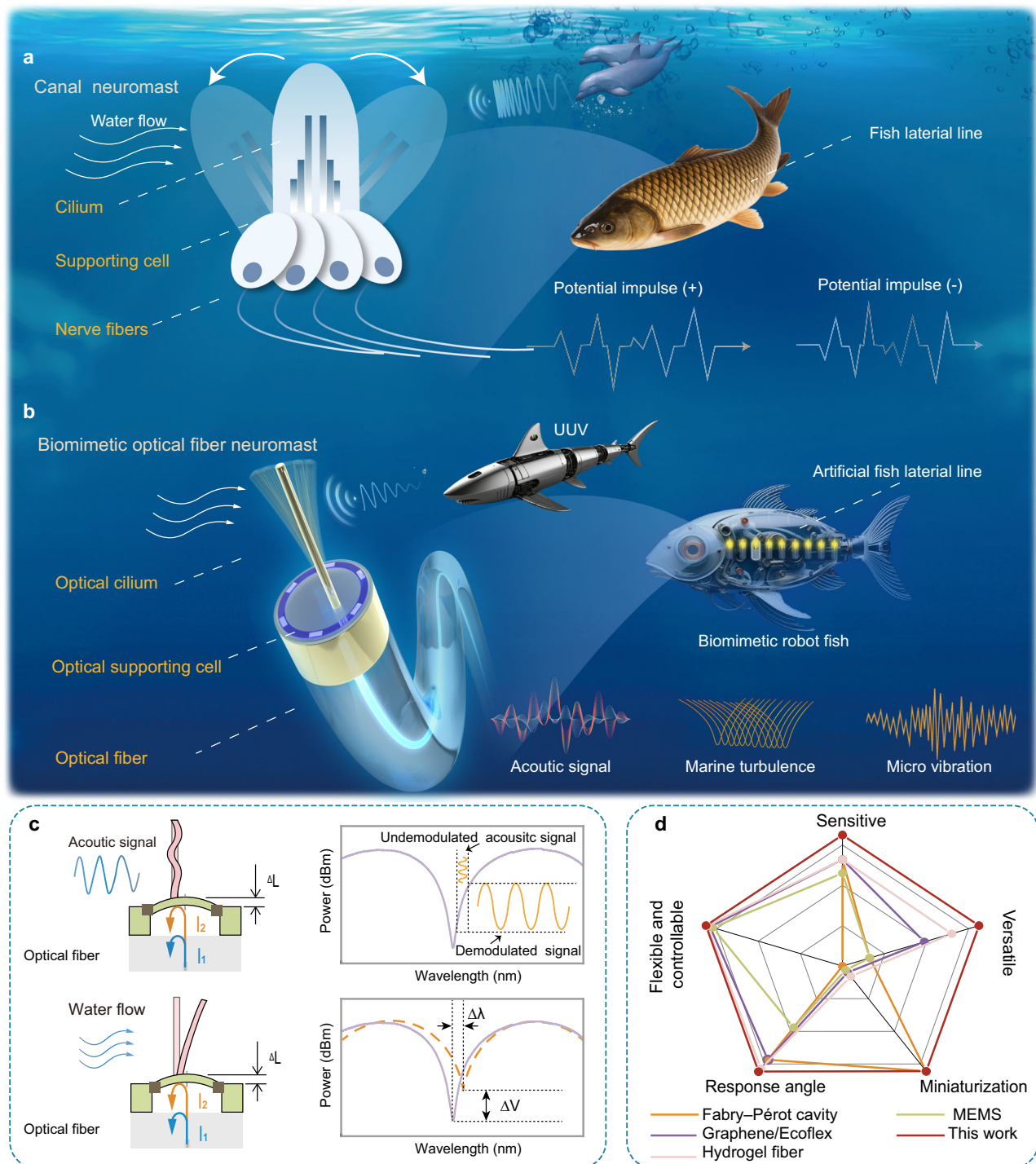


Fig. 1 | Schematic diagram of the biomimetic optical fiber neuromast (BOFN). **a** The Schematic drawings and working principle of the canal neuromast of the fish lateral line. **b** Illustration of the BOFN sensing external mechanical stimulation signals (UUV uncrewed underwater vehicles). **c** The working principle of detecting acoustic signals and water flow signals. **d** Technical comparison between BOFN and

published works utilizing Fabry-Pérot cavity, Graphene/Ecoflex Janus film, hydrogel fiber, and micro-electromechanical systems (MEMS) sensor for underwater sensing in terms of sensitivity, versatility, miniaturization, forward response angle, and adjustability.

Mechanical stimuli on the optical fiber neuromast are quantified by tracking the shift of the dip wavelength ($\Delta\lambda$) of the reflection spectrum. Hypotenuse intensity demodulation is used for high-frequency acoustic detection. To achieve maximum acoustic sensitivity, the laser is tuned to the optimal bias wavelength at the maximum slope of the interference spectrum, and the output power is modulated by the ultrasound wave. For low-frequency water flow detection, micro underwater vibrations are monitored by light

intensity variations (ΔV) (Fig. 1c). To our knowledge, the BOFN developed in this work is an all-optical biomimetic sensing cell, offering high sensitivity, tunability, multifunctionality, omni-directionality, and miniaturization adjustability^{19,30,37,38} (Fig. 1d, Supplementary Table 1).

Heterogeneous integration of BOFN

To meet the needs of underwater applications, we developed a self-designed heterogeneous integration process to integrate different

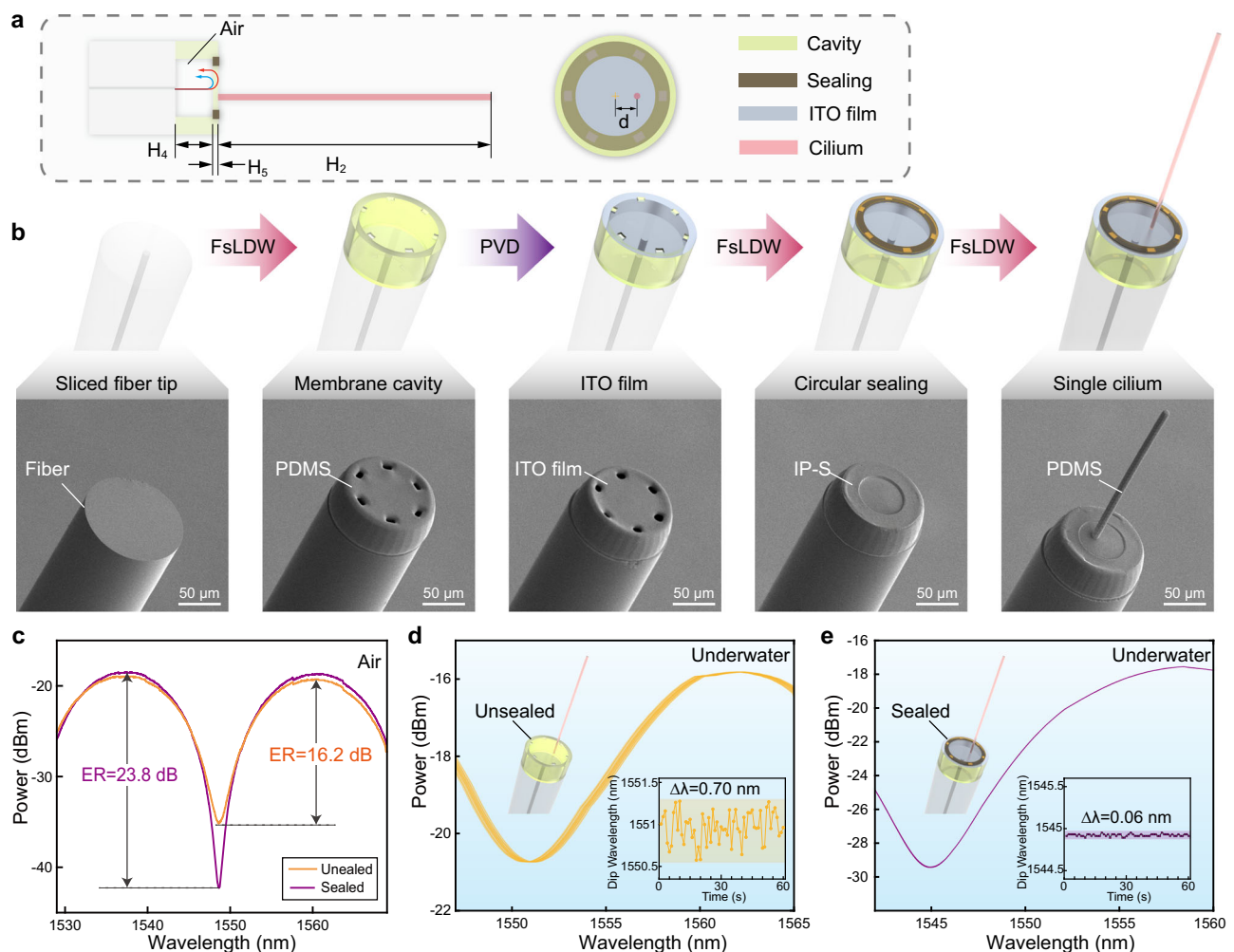


Fig. 2 | The integrated fabrication process of biomimetic optical fiber neuromast (BOFN). **a** Schematic of the proposed BOFN, showing its components and structural dimensions (ITO indium tin oxide). **b** Fabrication flow of the proposed BOFN, with SEM images displayed under each processing diagram (FsLDW femtosecond laser direct writing, PVD physical vapor deposition). **c** Underwater

interference spectrum of the unsealed and sealed optical supporting cell (ER extinction ratio). **d** Sixty-second monitoring of the underwater interference spectrum using the unsealed optical supporting cell. **e** Sixty-second monitoring of the underwater interference spectrum using the sealed optical supporting cell.

sensor components onto the tip of a fiber. The heterogeneous integration process combines femtosecond laser direct writing (FsLDW) and physical vapor deposition (PVD). FsLDW is implemented using a tightly focused femtosecond laser beam to induce nonlinear two-photon absorption in a photosensitive material, enabling precise polymerization of complex three-dimensional (3D) structures at the nanoscale (see details in the “Methods” section). By optimizing the processing parameters, such as laser power, scanning speed, and scanning scheme, it is possible to fabricate features with submicron resolution, ensuring the desired geometric and functional properties of the printed structures (see Supplementary Note 1 for details). This method allows the creation of stable, detailed, high-resolution microstructures from various composite materials. As depicted in Fig. 2a, the BOFN structure includes four key components: the cavity, sealing, indium tin oxide (ITO) film, and cilium. PDMS is used for the cavity and cilium to enhance sensitivity by efficiently transmitting vibrations with minimal energy loss. IP-S photoresist is used for sealing due to its low shrinkage, high stability, and suitability for TPP.

In detail, the heterogeneous integration of BOFN includes three steps of FsLDW and one step of PVD (Fig. 2b). First, a membrane cavity is created on the fiber tip using FsLDW with IP-PDMS photoresist. The thickness of the membrane film is optimized through parameter

adjustments, resulting in a stable process with a final thickness of 4 μm (Supplementary Fig. 2). Next, an ITO film is applied to the cavity using a DC-powered PVD device. The ITO film enhances adhesion between the PDMS surface and subsequent structures and improves interface reflectivity, thus increasing the reflected signal intensity. Third, the cavity is sealed using FsLDW with IP-S photoresist, creating an air cavity on the fiber tip. Rapid processing is essential once the fiber tip contacts the photoresist. The surface tension of small holes on the membrane cavity prevents the photoresist’s entry and seals the air cavity. Finally, a single cilium is fabricated on the cavity using FsLDW with photoresists like IP-S and IP-PDMS. The PDMS cilium achieved an aspect ratio of 30, highlighting the advanced technology of FsLDW on the fiber tip.

An experimental test of the underwater interference spectrum was conducted to assess the impact of the sealing design. During underwater testing, water entering the unsealed cavity reduces the refractive index, leading to a lower extinction ratio (ER) than the air cavity structure. As shown in Fig. 2c, the ER of sealed and unsealed FP cavities is 23.8 dB and 16.2 dB, respectively. Unsealed structures are also prone to noise interference from fluid disturbances, resulting in spectral drift. As presented in Fig. 2d, e, the spectral shift for sealed and unsealed FP cavities over 60 s is 0.70 and 0.06 nm. The comparative

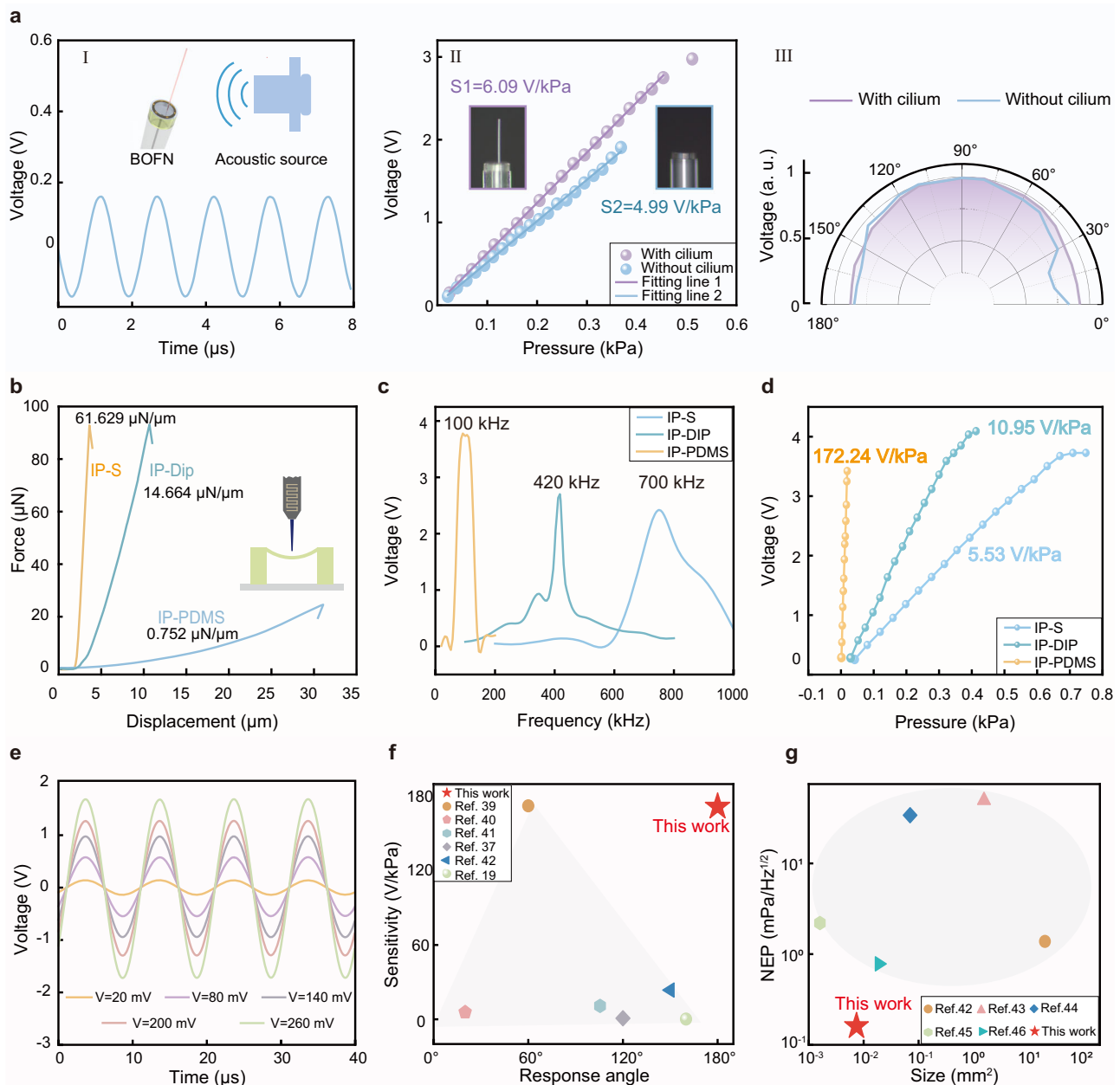


Fig. 3 | Acoustic signal sensing capability of the biomimetic optical fiber neuromast (BOFN). **a** Acoustic response of BOFN. **I** The acoustic time domain signal detected by IP-S BOFN. **II** Acoustic sensitivity from two structures. **III** Response angle from 0° to 180°. **b** Micro-nano mechanical response of three kinds of photoresist materials. **c** The frequency responses of BOFN made of three kinds of

materials. **d** The acoustic sensitivity of BOFN made of three kinds of materials. **e** The acoustic time domain signal detected by IP-PDMS BOFN. **f** Comparison of the sensitivity and forward response angle between the proposed BOFN and other current acoustic sensors. **g** Comparison of the noise equivalent pressure (NEP) and size between the proposed BOFN and other current acoustic sensors.

experiment demonstrates that the integrated fabrication of the BOFN significantly enhances spectral stability, achieving an order of magnitude improvement over the unsealed cavity. Leveraging the 3D fabrication capability of FsLDW, air cavities and high-aspect-ratio cilia are integrated on the fiber tip, showing promise for improving device performance.

Characterization of the acoustic signal measurements

The performance of the BOFN in ultrasound detection was first characterized. The demodulation system configuration of the ultrasound sensor is depicted in Supplementary Fig. 3. An external-cavity laser (model TSL710, Santec) with a narrow linewidth of <100 kHz and emitting wavelengths from 1480 to 1640 nm was used for

interrogation. It provided a high output power exceeding +10 dBm. To optimize sensitivity, the laser's pumping wavelength was tuned to coincide with the steepest slope of the resonances, ensuring a linear response from the BOFN. The reflected beams from the BOFN were measured simultaneously using a photodiode. To demonstrate the benefit of the sensory cilium, two sensor samples made with IP-S Nanoscribe photoresists were compared. The sample's response to sound waves at various frequencies was characterized. The acoustic time domain signal detected by the optical fiber neuromast is shown in Fig. 3a(I). The signal-to-noise (SNR) is 62.06 dB, and the corresponding noise equivalent pressure (NEP) is estimated as 19.29 mPa ($192.9 \mu\text{Pa Hz}^{-1/2}$) (Supplementary Fig. 4). The sensitivity and response time of the BOFN is calibrated under static water conditions at room

temperature of 20–25 °C and water depth of 15 cm (Supplementary Fig. 5) Sensitivity calibration was performed using a piezoelectric ceramic transducer (PZT) (Olympus, V318) immersed in water. The BOFN was placed about 30 mm against the PZT, driven by a sinusoidal voltage signal generator. The optical neuromast exhibited a sensitivity of 6.09 V/kPa (Fig. 3a(II)). In addition, the forward-direction response was also evaluated. During this measurement, the BOFN was fixed as the rotation center, and ultrasound signals were applied at 3 cm from the probe, with angles ranging from 0° to 180° in 10° increments. The BOFN had a wide detection angle of 0–180° (Fig. 3a(III)). It confirmed that the BOFN could detect all the induced signals and had a uniform sensitivity at 180° in front of the BOFN. In comparison, the ordinary FP structure without the cilium displays the acoustic signal with an SNR of 56.87 dB, a center frequency of 600 kHz, a sensitivity of 4.99 V/kPa, and an NEP of 30.21 mPa (302.1 $\mu\text{Pa Hz}^{-1/2}$) (Fig. 3a II, Supplementary Fig. 6). In addition, the acoustic response of the transducer is non-uniform from 0° to 180°. (Fig. 3a III). Therefore, the BOFN with the cilium structure demonstrated improved SNR and sensitivity, a notable reduction in NEP, and a more uniform directional response.

To investigate how different photoresist types affect BOFN sensing performance, three photoresists were tested in the heterogeneous integration process (Supplementary Table 2). First, the mechanical properties of the three materials were tested (Fig. 3b). When an axial force was applied to the thin film cavity, the film shifted due to the microforce probe, causing a change in cavity length. The flexible PDMS thin film micro-cavity showed greater sensitivity to cavity length changes under external force (Supplementary Fig. 7). A finite element method (FEM) model was employed to evaluate the BOFN's responses to external acoustic pressure across the three different materials. The IP-PDMS material showed a sensitivity approximately 20 times as high as that of the IP-S material (Supplementary Fig. 8). Figure 3c, d illustrates the sensitivity and frequency response of optical fiber neuromasts made from IP-S, IP-DIP, and IP-PDMS. The IP-PDMS sample exhibited superior sensitivity, while the IP-S sample demonstrated the highest center frequency. The acoustic time domain signal detected by the PDMS optical fiber neuromast is demonstrated in Fig. 3e. An increase in the driving voltage of the signal generator results in a greater amplitude of the acoustic signal. The IP-PDMS BOFN detected acoustic signals with an SNR of 42.06 dB and an NEP of 11.52 mPa (162.92 $\mu\text{Pa Hz}^{-1/2}$) (Supplementary Fig. 9). Moreover, the BOFN outperforms existing acoustic sensors in sensitivity, response angle, and NEP by orders of magnitude^{19,37,39–46} (Fig. 3f, g, Supplementary Tables 3–5).

Responses to water flow stimuli and underwater communication detection

Benefiting from the sensitive and uniform performance of the optical fiber neuromast, it was further used to achieve underwater wake and disturbance detection. Initially, the IP-PDMS BOFN was used to detect marine turbulence in a laboratory simulation (Supplementary Fig. 10). Figure 4a depicts the alteration in dip wavelength in response to a gradual increase in water velocity, ranging from 60 to 120 $\mu\text{L}/\text{min}$ in increments of 20 $\mu\text{L}/\text{min}$. As the velocity rises, the dip wavelength exhibits a redshift. The sensitivity is determined based on the slopes of the dip wavelength relative to the flow velocity. As Fig. 4b illustrates, the sensitivity is calculated as 45.42 pm/($\mu\text{L}/\text{min}$), corresponding to 8560.72 nm/(m/s). The wavelength interrogator has a resolution of 0.02 nm, translating to a velocity resolution of 2.34 $\mu\text{m}/\text{s}$. The BOFN outperforms the existing flow sensors in both sensitivity and resolution^{47–54} (Fig. 4c, Supplementary Table 6). To further demonstrate its underwater perception capabilities, the optical fiber neuromast can sense both minor and intense mechanical stimuli in water. The device had the ability to perceive vibrations or fluctuations in the water surface caused by natural fallen objects such as leaves, metal, and stones (Fig. 4d). It detected 1 g weights dropped from various

heights and different amounts of water droplets (Supplementary Fig. 11). Besides, the BOFN detected signals of varying frequencies generated by striking the ground with a hammer (Fig. 4e). It can also sense the fall and rebound process of a steel ball. Figure 4f records the optical intensity variation during the fall and rebound process, and the relative voltage change is related to the rebound height of the ball.

The increased utilization of marine resources has led to a growing focus on underwater communication, which serves not only to transmit information but also to enhance the safety of underwater vehicles. For instance, deep-sea vehicles may require the ability to call for emergency assistance. In this work, inspired by the capability of detecting tiny vibrations, the proposed BOFN has been employed for Morse code communication in underwater environments. According to Fig. 4g, each letter in the English alphabet can be encoded through sequences comprising two distinct signals: dots and dashes. The word “HUST” can be transmitted through flowing water using sequences of short and long durations, according to Morse code principles (Fig. 4h). In addition, the BOFN possessed the capability to transmit an “SOS” distress signal utilizing Morse code in the event of an emergency. Even with artificial noise interference, the “SOS” signal could be accurately decoded, which proved the robustness of underwater communication (Supplementary Fig. 12). We believe the communication capabilities of BOFN in aquatic environments hold significant potential for ocean exploration.

Demonstration of an artificial bionic fish lateral line for underwater perception

Figure 5a illustrates an ocean monitoring system that integrates IP-S BOFN and IP-PDMS BOFN into a robotic fish. This system enables BOFN to detect both high-frequency acoustic signals (HFS) and low-frequency water flow disturbance signals in underwater environments. Biomimetic robotic fish's ability to detect HFS not only allows it to track underwater mammals and UUVs but also enables active imaging of underwater targets, such as jellyfish, coral reefs, or submerged structures. Additionally, biomimetic robotic fish can detect low-frequency signals generated by ocean wakes, ship traffic, and other environmental phenomena, offering a comprehensive monitoring solution. This enhancement illustrates biomimetic robotic fish versatility for real-time marine monitoring and imaging applications, demonstrating its potential for both ecological studies and environmental assessments. To assess its comprehensive underwater sensing capabilities, optical fiber neuromasts were mounted on a motorized fish to simultaneously measure high-frequency acoustic and low-frequency water flow signals (Fig. 5b, Supplementary Fig. 13). A piezoelectric ultrasonic transducer, driven by a function generator, was attached to a model shark to generate ultrasonic signals. The model shark was remotely controlled. Figure 5c presents the acoustic signals from the moving model shark detected by the motorized fish. The model shark emitted acoustic signals at frequencies of 500 kHz at various locations. In addition, motorized fish also detected the water mechanical stimuli caused by the movement of the model shark (Fig. 5d). Figure 5e displays the acoustic signals at the frequencies of 400, 600, and 800 kHz recorded by both the hydrophone and bionic motorized fish with BOFN. The waveform amplitude from the hydrophone was much lower than that of the bionic fish. The short-time Fourier transform analysis was further used to verify the frequency signals from the hydrophone and the bionic fish. The results were highly consistent in the frequency domain (Supplementary Fig. 14).

To illustrate the practical use of ultrasound imaging, the bionic fish with BOFN was developed. The ultrasound wave emitted by the PZT will pass through the object and be received by the bionic fish. The bionic fish scanned the target point by point to realize the multi-point detection of the object. The high-resolution jellyfish images were reconstructed by the peak-to-peak image reconstruction technique (Fig. 5f). The bionic fish's capacity for underwater imaging was further

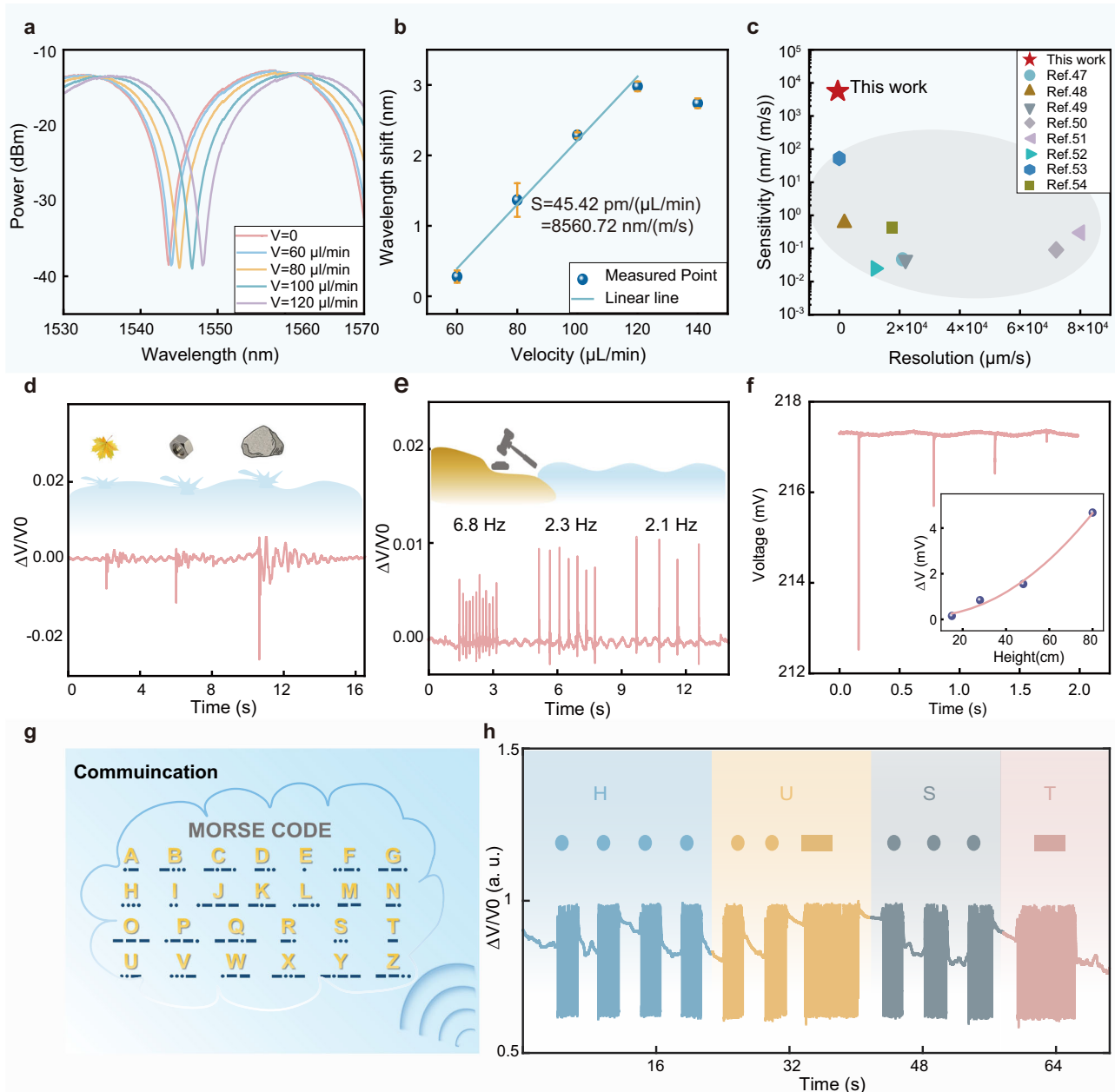


Fig. 4 | Water flow mechanical stimulation response of the BOFN. a Variation in the reflection spectra of the BOFN. **b** Relationship between dip wavelength and flow velocity. The error bars denote the different wavelength shifts obtained at the same velocities. **c** Comparison of the proposed BOFN and existing flow velocity sensors regarding sensitivity and resolution. **d** The BOFN's response to a falling leaf, metal,

and stone. **e** The BOFN's response to percussion stimulation at varying frequencies. **f** The BOFN's response to stimulation from a steel ball falling from different heights. **g** Application scenarios of underwater Morse code communication. **h** Transmitting Morse code for the word "HUST".

demonstrated by imaging both starfish and fish models. (Supplementary Fig. 15). Moreover, the motion state of the motorized fish can be controlled remotely. Consequently, the BOFN effectively monitored the different movement states of swimming motorized fish, whether fast swinging or slow swinging, demonstrating significant potential in underwater monitoring applications (Fig. 5g). The swinging frequency of motorized fish was 12.53 Hz and 4.21 Hz, respectively (Supplementary Fig. 16).

Discussion

In summary, we present a proof-of-concept prototype of a bioinspired optical fiber neuromast, designed to mimic the fish lateral line system. This artificial neuromast features an optical supporting cell for

mechanical-optical transduction, a photoresist micro-cilium acting as a cantilever beam, and an optical fiber for signal transmission. The heterogeneous integration structure constructed by the sequential FSLDW with deposition technique enables the high-performance bioinspired optical fiber neuromast, which has a simpler configuration than its analogs. The biomimetic device effectively detects various underwater signals, including ultrasound signals with different frequencies, marine turbulence velocities, and vibrations from multiple directions. The BOFN achieves excellent acoustic sensitivity of 172.24 V/kPa (NEP 162.92 $\mu\text{Pa} \cdot \text{Hz}^{-1/2}$), a wide-angle response of 0–180°, and marine turbulence velocity sensitivity of 45.42 pm/($\mu\text{L}/\text{min}$) corresponding to 8560.72 nm/(m/s). Moreover, various stimuli, such as water drops, vibration, and Morse code signals, are well detected. It

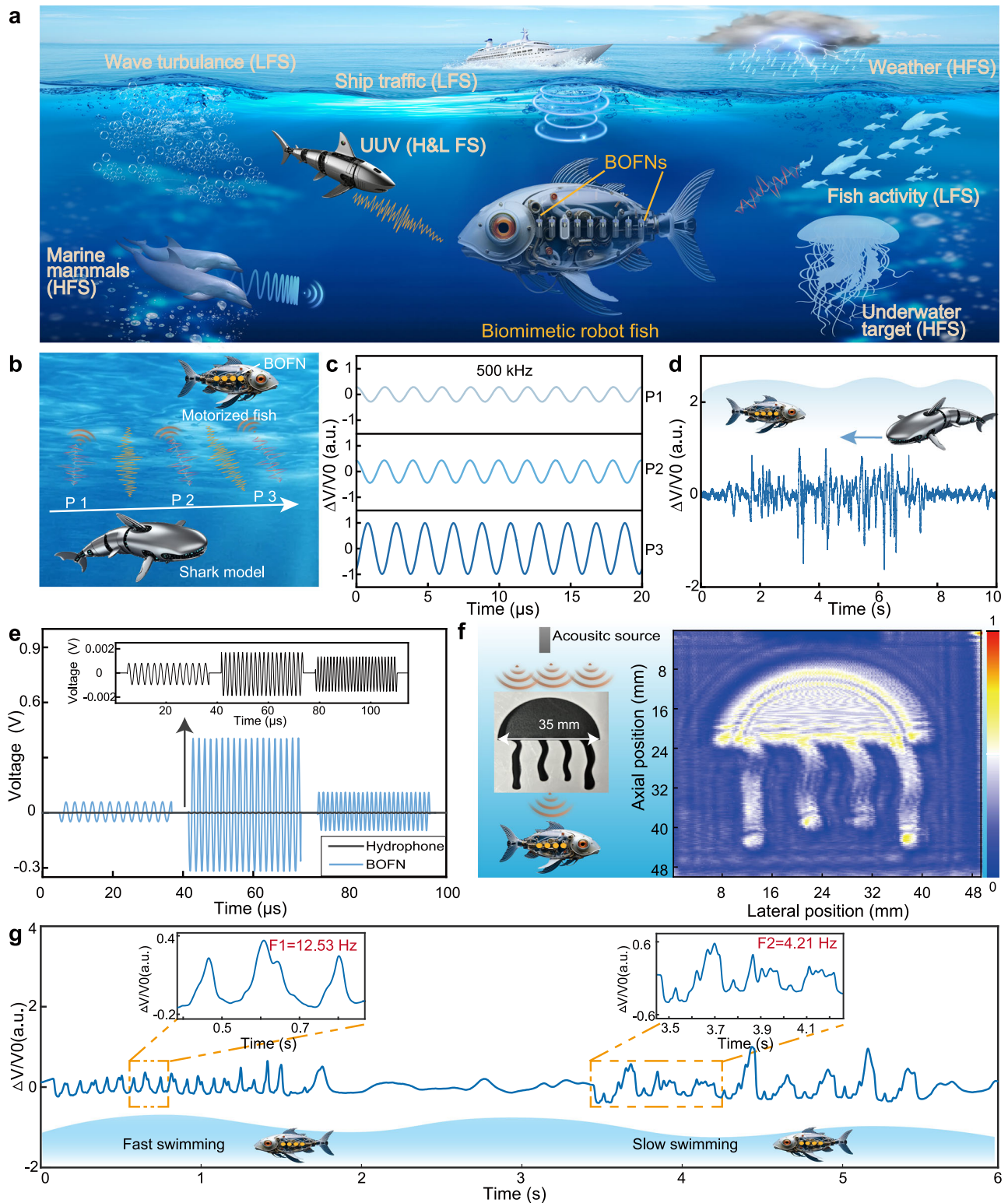


Fig. 5 | Integrated application of underwater detection. **a** The conceptual diagram of an ocean monitoring system based on biomimetic optical fiber neuromast (BOFN) (HFS high-frequency acoustic signals, LFS low-frequency water flow disturbance signals). **b** The application scenario diagram showing the model shark emitting sound waves at different locations as it swims. **c** The acoustic signals detected by the motorized fish during the movement of the model shark. **d** The

water flow mechanical stimulation signals detected by the motorized fish as the shark moves. **e** The acoustic signals recorded by both the hydrophone and BOFN, demonstrating that BOFN exhibits higher sensitivity. **f** Reconstructed cross-section image of jellyfish objects obtained through ultrasound imaging by the bionic fish. **g** Real-time changes in optical attenuation of the BOFN attached to the moving motorized fish, reflecting the fish's movement at various speeds.

provides detailed information on the strength, frequency, and spectral profiles of the detected signals, including peaks and pulses. Benefiting from the compact size ($\varnothing = 125\ \mu\text{m}$, $h = 340\ \mu\text{m}$), the BOFN's performance is further showcased by its integration into a motorized fish, which enables diverse detection capabilities and underwater imaging.

For comparison, traditional underwater sensors are often bulky, with low sensitivity and limited directionality, which restricts their application in fully bionic systems. The bioinspired 3D bionic design and heterogeneous integration process enable the creation of BOFN that mimics both the structure and function of the canal neuromast in the fish lateral line. This bioinspired design marks a significant improvement over existing sensors, offering enhanced angle response and greater sensitivity, as well as the SNR and resolution (Supplementary Table 7). Notably, the bionic motorized fish can detect both low and high-frequency signals simultaneously. Additionally, BOFN achieves multi-dimensional integration in function and scale, expanding its practical applications to underwater early warning, navigation, and marine exploration. Further improvements in the sensor's directivity and sensitivity can be achieved by adding a gradient ciliary array. Using biocompatibility material, the BOFN may be integrated into a live fish to realize more covert sensing. The biomimetic device has potential applications in wireless monitoring of underwater parameters in remote marine locations, offering marine organisms, underwater vehicles, and the possibility of incorporating responsive components for specific detections. The BOFN system also exhibits significant potential for broad application across diverse fields, including robotics, biomedical devices, and environmental monitoring, showcasing its adaptability to address multifaceted challenges^{55,56} (Supplementary Note 2). To fully realize these diverse applications, especially in challenging marine environments, it is essential to consider the operational and environmental conditions. The maximum pressure validated in the current tests was 3 MPa (equivalent to ~300 m underwater) due to experimental condition constraints, while this is sufficient for many shallow and mid-depth marine applications. Further enhancement of pressure testing conditions and continued improvement of material encapsulation are anticipated to enable reliable operation in deep-sea environments. Simultaneously, these advancements will drive progress in integrating the sensor and the organism, as well as active ocean detection.

Methods

Sensor fabrication process

A custom-built FsLDW system was employed to fabricate the membrane cavity and seal on the fiber tip. The system utilized a femtosecond mode-locked Ti: sapphire laser (Coherent, Chameleon Discovery, 100 fs pulse width, 80 MHz repetition rate) and a 40 \times , NA 1.3 objective (Olympus, UPLFLN 40XO) for all processing steps. The laser beam was guided through a 4f imaging system combined with 2D galvo mirrors (SCANLAB, IntelliSCAN III 14) and tightly focused within the sample. Laser power was modulated using an acoustic-optic modulator (AA, MT110-B50A1.5-IR-Hk), and an X-Y-Z piezo stage (Physik Instrument, P-563.3CD) controlled the precise scanning movements of the focused laser spot. Initially, a membrane cavity was fabricated on the sliced fiber tip using the IP-PDMS photoresist. The FsLDW parameters for the main structure were laser power 45 mW, scanning speed 60 mm \cdot s⁻¹, hatching distance 0.3 μm , and slicing distance 0.3 μm . The FsLDW parameters were: laser power 45 mW, scanning speed 60 mm \cdot s⁻¹, hatching distance 0.3 μm , and slicing distance 0.3 μm . Holes were incorporated into the design to ensure proper development between the capillary tip and the piston. Post-printing, the development process in IPA for 12 min was conducted to remove uncured photoresist. A thin film of ITO, 5 nm thick, was deposited onto the cavity using a DC sputtering system (FANGSHENG, FS450). Subsequently, a circular sealing was fabricated on the coated membrane cavity using the IP-S photoresist. The FsLDW parameters for the sealing were laser power

32.5 mW, scanning speed 100 mm s⁻¹, hatching distance 0.3 μm , and slicing distance 0.5 μm . The printed IP-S structure was then developed in PGMEA for 5 min, followed by IPA for 3 min to remove the uncrosslinked resin. Finally, a single cilium was fabricated on the sealed cavity using the IP-PDMS photoresist under main FsLDW parameters of laser power 50 mW, scanning speed 60 mm s⁻¹, hatching distance 0.3 μm , and slicing distance 0.3 μm . After printing, the entire fiber tip was developed in IPA for 10 min to eliminate uncrosslinked resin. A detailed description of the laser processing parameters for the various components of the BOFN is provided in Supplementary Fig. 17 and Supplementary Table 8. A discussion on the scalability of the fabrication process is provided in Supplementary Note 3, and a detailed cost analysis of BOFN fabrication is provided in Supplementary Note 4 and Supplementary Table 9. The results of repetitions and the margin of error demonstrate the reproducibility of the fabrication process (Supplementary Fig. 18, Supplementary Table 10, and Table 11).

Material characterization

Scanning electron microscopy (SEM) images were obtained using a field-emission SEM (FEI, Nova Nano SEM450) at an acceleration voltage of 10 kV. Optical images were captured with a laser confocal microscope (Keyence, VK-X1100). The compression test of the membrane film was performed using a micromechanical testing system (Femto-Tools, FT-MTA02). An FT-S1000 micro force sensing probe was employed with a force range of $\pm 1000\ \mu\text{N}$ and a resolution of 0.05 μN . The probe features a tungsten tip with a radius of <2 μm and a length of $2.5 \pm 0.5\ \mu\text{m}$.

Experimental setup

A schematic of the multifunction test experimental setup is shown in Supplementary Fig. 19. A tunable laser (Santec, TSL-710) emits interrogation light, which enters the IP-S BOFN through a circulator (Guanglin OFCIR-15-A-1). An amplified spontaneous emission (ASE) light source (ASE-1550-15-SM, Beijing Zhongxun Spectrum Technology Limited Company, China) transmits broadband light through another circulator into the IP-PDMS BOFN. For low-frequency mechanical stimulus detection, the photodetector (APD, Thorlabs APD430) converts the optical signal into an electrical signal and transmits it to the signal acquisition and processing unit. The signal is then processed through a low-pass filter to obtain the water stimulation signal. For high-frequency acoustic detection, when an ultrasound wave interacts with the sensor, it modulates the reflected beam's intensity. A balanced detector photodetector (BPD, Optolabs PD-100MA) captures this reflected beam and converts it into an electrical signal, from which both direct current (DC) and alternating current (AC) components are extracted. The DC component is sent to DAQ2 (NI USB-6002) for analysis on the PC, while the AC component is directed to DAQ1 (PCIE 8586) to output the ultrasound signal. The PC analyzes the DC signals to determine the optimal wavelength corresponding to the maximum slope of the sensor's reflectance spectrum, optimizing the sensitivity of the ultrasound sensing system. This optimal wavelength information is then returned to the tunable laser for adjustment. The ultrasound wave modulates the output power of the wavelength.

Durability and practical use

To evaluate the environmental durability and performance of the BOFN, we conducted extensive testing focused on their respective applications: high-frequency acoustic imaging using the IP-S BOFN and low-frequency water flow disturbance detection using the IP-PDMS BOFN. Laboratory demonstrations were performed to replicate real-world underwater conditions, including salinity variations (30–35‰), temperature fluctuations, biofouling, and mechanical stress (Supplementary Figs. 20–27). Long-term stability testing over a 4-week period demonstrated the IP-S BOFN's ability to maintain accurate imaging of a jellyfish model and the IP-PDMS BOFN's consistent detection of

motorized fish movements and 2 g weight drops in simulated seawater (Supplementary Figs. 28–31). Additionally, the IP-PDMS BOFN underwent 20,000 vibration cycles to confirm its mechanical stability (Supplementary Figs. 32, 33). To validate real-world performance, field tests were conducted in the East Lake of Wuhan, China, where the IP-PDMS BOFN effectively monitored ripple signals, low-frequency disturbances, and the motion of motorized fish in natural aquatic environments (Supplementary Figs. 34–36). Simulated deep-sea pressure testing was carried out in a specialized hydraulic pressure cylinder (Supplementary Figs. 37, 38). These comprehensive tests highlight the durability, reliability, and adaptability of the BOFN in diverse and challenging underwater environments.

Data availability

The data generated in this study are provided in the Source Data file.

References

- Picardi, G. et al. Bioinspired underwater legged robot for seabed exploration with low environmental disturbance. *Sci. Robot.* **5**, eaz1012 (2020).
- Zhou, Y. et al. A multimodal magnetoelastic artificial skin for underwater haptic sensing. *Sci. Adv.* **10**, eadj8567 (2024).
- Katzschmann, R. K., DelPreto, J., MacCurdy, R. & Rus, D. Exploration of underwater life with an acoustically controlled soft robotic fish. *Sci. Robot.* **3**, eaar3449 (2018).
- Jain H. & Patankar V. Embedded system for ultrasonic imaging of under-water concrete structures. *J. Instrum.* **16**, P 07049(2021).
- Yu, J. et al. Molecular architecture regulation for the design of instant and robust underwater adhesives. *Sci. Adv.* **9**, eadg4031 (2023).
- John, F., Cimdins, M. & Hellbrück, H. Underwater ultrasonic multi-path diffraction model for short range communication and sensing applications. *IEEE Sens. J.* **21**, 22934–22943 (2021).
- Wang, T. et al. A versatile jellyfish-like robotic platform for effective underwater propulsion and manipulation. *Sci. Adv.* **9**, eadg0292 (2023).
- Powell, S. B., Garnett, R., Marshall, J., Rizk, C. & Gruev, V. Bioinspired polarization vision enables underwater geolocalization. *Sci. Adv.* **4**, eaao6841 (2018).
- Connors, M. et al. Bioinspired design of flexible armor based on chiton scales. *Nat. Commun.* **10**, 5413 (2019).
- Krieg, M., Nelson, K. & Mohseni, K. Distributed sensing for fluid disturbance compensation and motion control of intelligent robots. *Nat. Mach. Intell.* **1**, 216–224 (2019).
- Li, Y. et al. An all-optical multidirectional mechano-sensor inspired by biologically mechano-sensitive hair sensilla. *Nat. Commun.* **15**, 2906 (2024).
- Mogdans, J. Sensory ecology of the fish lateral-line system: morphological and physiological adaptations for the perception of hydrodynamic stimuli. *J. Fish. Biol.* **95**, 53–72 (2019).
- Lee, K. Y. et al. An autonomously swimming biohybrid fish designed with human cardiac biophysics. *Science* **375**, 639–647 (2022).
- Pyun, J. Y., Kim, Y. H. & Park, K. K. Design of piezoelectric acoustic transducers for underwater applications. *Sensors* **23**, 1821 (2023).
- Zhang, Q. et al. Multifunctional and wearable patches based on flexible piezoelectric acoustics for integrated sensing, localization, and underwater communication. *Adv. Funct. Mater.* **33**, 2209667 (2023).
- Lyu, C. et al. Bone-inspired (GNEC/HAPAAm) hydrogel with fatigue-resistance for use in underwater robots and highly piezoresistive sensors. *Microsyst. Nanoeng.* **9**, 99 (2023).
- Wei, Y. et al. Fully paper-integrated hydrophobic and air permeable piezoresistive sensors for high-humidity and underwater wearable motion monitoring. *npj Flex. Electron.* **7**, 13 (2023).
- Yang, L. et al. Comparison survey of effects of hull on AUVs for underwater capacitive wireless power transfer system and underwater inductive wireless power transfer system. *IEEE Access* **10**, 125401–125410 (2022).
- Wang A. et al. Three-dimensional-printed hollow Fabry-Perot fiber sensor for ultra-high sensitivity ultrasound detection. In *Proc. Optical Fiber Communication Conference and Exhibition (OFC)* (IEEE, 2024).
- Gao, S. et al. Model test research of wave-induced submarine landslide based on Fibre Bragg Grating sensing technology. *Ocean Eng.* **291**, 116492 (2024).
- Chen, C. et al. Shape monitoring method of submarine cable based on fiber Bragg grating. *Optical Fiber Technol.* **77**, 103255 (2023).
- Sang, G. et al. A compact multifunctional fiber sensor for simultaneous underwater measurement of salinity, temperature and strain. *Measurement* **194**, 111039 (2022).
- Fan, P. et al. High sensitivity fiber-optic Michelson interferometric low-frequency acoustic sensor based on a gold diaphragm. *Opt. Express* **28**, 25238–25249 (2020).
- Zhao, W. et al. A Sagnac-based interferometer with optimal polarization control for Lamb wave detection. *Opt. Laser Technol.* **143**, 107325 (2021).
- Wei, H. et al. Two-photon 3D printed spring-based Fabry-Pérot cavity resonator for acoustic wave detection and imaging. *Photonics Res.* **11**, 780–786 (2023).
- Xiong, W. et al. Sensitivity enhanced fiber optic hydrophone based on an extrinsic Fabry-Perot interferometer for low-frequency underwater acoustic sensing. *Opt. Express* **30**, 9307–9320 (2022).
- Yao, M. et al. Ultracompact optical fiber acoustic sensors based on a fiber-top spirally-suspended optomechanical microresonator. *Opt. Lett.* **45**, 3516–3519 (2020).
- Shang X. et al. Customizable and highly sensitive 3D micro-springs produced by two-photon polymerizations with improved post-treatment processes. *Appl. Phys. Lett.* **120**, 171107 (2022).
- Zhang, W. et al. Vector high-resolution marine turbulence sensor based on a MEMS bionic cilium-shaped structure. *IEEE Sens. J.* **21**, 8741–8750 (2020).
- Wang, Q., Xiao, P., Zhou, W., Liang, Y. & Yin, G. Bioinspired adaptive, elastic, and conductive graphene structured thin-films achieving high-efficiency underwater detection and vibration perception. *Nano-Micro Lett.* **14**, 62 (2022).
- Yang, B., Zhang, T., Liang, Z. & Lu, C. Research on an artificial lateral line system based on a bionic hair sensor with resonant readout. *Micromachines* **10**, 736 (2019).
- Hu Q., Liu Y., Zhao Z. Y. & Lei Z. F. Intelligent detection for artificial lateral line of bio-inspired robotic fish using EMD and SVMs. In *Proc. IEEE International Conference on Robotics and Biomimetics (ROBIO)* (IEEE, 2018).
- Li, Z., Myung, N. V. & Yin, Y. Light-powered soft steam engines for self-adaptive oscillation and biomimetic swimming. *Sci. Robot.* **6**, eabi4523 (2021).
- Zhu, W. et al. Surface plasmon polariton laser based on a metallic trench Fabry-Perot resonator. *Sci. Adv.* **3**, e1700909 (2017).
- Gao, F., Liao, W.-H. & Wu, X. Being gradually softened approach for solving large deflection of cantilever beam subjected to distributed and tip loads. *Mech. Mach. Theory* **174**, 104879 (2022).
- Zou, M. et al. Fiber-tip polymer clamped-beam probe for high-sensitivity nanoforce measurements. *Light. Sci. Appl.* **10**, 171 (2021).
- Fan, Q. et al. MEMS piezoelectric bionic directional sound sensor based on ZnO thin film. *Sens. Actuators A Phys.* **347**, 113971 (2022).
- Wang, C., Wu, B., Sun, S. & Wu, P. Interface deformable, thermally sensitive hydrogel-elastomer hybrid fiber for versatile underwater sensing. *Adv. Mater. Technol.* **5**, 2000515 (2020).

39. Zhang, L. et al. High-sensitivity fiber optic Fabry–Perot ultrasonic sensor based on a grooved silicon diaphragm for partial discharge detection. *Appl. Opt.* **62**, 6809–6815 (2023).
40. Yang, H. et al. AlScN film based piezoelectric micromechanical ultrasonic transducer for an extended long-range detection. *Micromachines* **13**, 1942 (2022).
41. Tu, X. et al. Underwater acoustic wave detection based on packaged optical microbubble resonator. *J. Light. Technol.* **40**, 6272–6279 (2022).
42. Wang, Y. et al. A lever-type PDMS flexible cavity for acoustic vector sensor with high sensitivity. *IEEE Sens. J.* **23**, 5637–5642 (2023).
43. Li, C. et al. D-shaped fiber Bragg grating ultrasonic hydrophone with enhanced sensitivity and bandwidth. *J. Light. Technol.* **37**, 2100–2108 (2019).
44. Yang, L. et al. Highly sensitive and miniature microfiber-based ultrasound sensor for photoacoustic tomography. *Opto-Electron. Adv.* **5**, 200076 (2022).
45. Pan, J. et al. Parallel interrogation of the chalcogenide-based micro-ring sensor array for photoacoustic tomography. *Nat. Commun.* **14**, 3250 (2023).
46. Liu Y. et al. Acoustic-optomechanical oscillator for low noise equivalent pressure and large broadband response acoustic sensing applications. *Appl. Phys. Lett.* **124**, 072202 (2024).
47. Wang, X. et al. Optical fiber anemometer using silver-coated fiber Bragg grating and bitaper. *Sens. Actuators A Phys.* **214**, 230–233 (2014).
48. Wang, X. et al. Hot-wire anemometer based on silver-coated fiber Bragg grating assisted by no-core fiber. *IEEE Photonics Technol. Lett.* **25**, 2458–2461 (2013).
49. Dong, X., Zhou, Y., Zhou, W., Cheng, J. & Su, Z. Compact anemometer using silver-coated fiber Bragg grating. *IEEE Photonics J.* **4**, 1381–1386 (2012).
50. Wang, J. et al. Fiber-optic anemometer based on Bragg grating inscribed in metal-filled microstructured optical fiber. *J. Light. Technol.* **34**, 4884–4889 (2016).
51. Caldas, P. et al. Fiber optic hot-wire flowmeter based on a metallic coated hybrid long period grating/fiber Bragg grating structure. *Appl. Opt.* **50**, 2738–2743 (2011).
52. Gao, S., Zhang, A. P., Tam, H.-Y., Cho, L. & Lu, C. All-optical fiber anemometer based on laser heated fiber Bragg gratings. *Opt. Express* **19**, 10124–10130 (2011).
53. Liu G., Sheng Q., Piassetta G. R. L., Hou W. & Han M. A fiber based on laser-heated silicon Fabry–Pérot cavity. In *Fiber Optic Sensors and Applications XIII*, Proc. SPIE 9852 (2016).
54. Costa, J. W., Franco, M. A., Serrão, V. A., Cordeiro, C. M. & Giraldo, M. T. Macrobending SMS fiber-optic anemometer and flow sensor. *Opt. Fiber Technol.* **52**, 101981 (2019).
55. Afzal, S. S. et al. Battery-free wireless imaging of underwater environments. *Nat. Commun.* **13**, 5546 (2022).
56. Liu, K. et al. A maneuverable underwater vehicle for near-seabed observation. *Nat. Commun.* **15**, 10284 (2024).

Acknowledgements

This work was supported by the National Natural Science Foundation of China (grants no. 62425505 to Q.S., grant no. 623B2034 to L.L., and

grant no. 52275429 to W.X.), the Hubei Natural Science Foundation Innovative Research Group Project (grant no. 2024AFA025 to W.X.), and the Fundamental Research Funds for the Central Universities (grant no. 2024BRA012 to Q.S.). We thank Prof. Yinshui Liu and Mr. Tianhao Li for their assistance with experimental tests.

Author contributions

L.L. and X.F. contributed equally to this work. Q.S. and W.X. conceived the project. L.L. and X.F. fabricated the device. L.L. and X.F. carried out the data collection. G.C. and Y.L. designed the imaging system. F.Z. and Z.Z. conducted the simulation study. Z.C., S.Z. and W.X. designed the theoretical model. L.L., Z.L. and Z.Y. conducted data analysis. Q.S., W.X., H.G. and Y.L. participated in the discussion of results, with all authors contributing to the discussion and preparation of the manuscript.

Competing interests

The authors declare no competing interests.

Additional information

Supplementary information The online version contains supplementary material available at <https://doi.org/10.1038/s41467-025-62559-3>.

Correspondence and requests for materials should be addressed to Wei Xiong or Qizhen Sun.

Peer review information *Nature Communications* thanks Yongfeng Lu and Jeonghyun Ki for their contribution to the peer review of this work. A peer review file is available.

Reprints and permissions information is available at <http://www.nature.com/reprints>

Publisher's note Springer Nature remains neutral with regard to jurisdictional claims in published maps and institutional affiliations.

Open Access This article is licensed under a Creative Commons Attribution-NonCommercial-NoDerivatives 4.0 International License, which permits any non-commercial use, sharing, distribution and reproduction in any medium or format, as long as you give appropriate credit to the original author(s) and the source, provide a link to the Creative Commons licence, and indicate if you modified the licensed material. You do not have permission under this licence to share adapted material derived from this article or parts of it. The images or other third party material in this article are included in the article's Creative Commons licence, unless indicated otherwise in a credit line to the material. If material is not included in the article's Creative Commons licence and your intended use is not permitted by statutory regulation or exceeds the permitted use, you will need to obtain permission directly from the copyright holder. To view a copy of this licence, visit <http://creativecommons.org/licenses/by-nc-nd/4.0/>.

© The Author(s) 2025